Estimating gas saturation in a thin layer by using frequency-dependent amplitude versus offset modelling

Estimating gas saturation in a thin layer by using frequency-dependent amplitude versus offset modelling

Zhaoyu Jin[1, *], Mark Chapman[1], Xiaoyang Wu[2] and Giorgos Papageorgiou[1]

1. School of GeoSciences, The University of Edinburgh, Grant Institute, James Hutton Road, Edinburgh, EH9 3FE, UK.

2. Edinburgh Anisotropy Project, British Geological Survey, The Lyell Centre, Research Avenue South, Edinburgh, EH14 4AP, UK.

* E-mail: Zhaoyu.Jin@ed.ac.uk

Abstract

Various models have been proposed to link partial gas saturation to seismic attenuation and dispersion, suggesting that the reflection coefficient should be frequency-dependent in many cases of practical importance. Previous approaches to studying this phenomenon have typically been limited to single interface models. Here we propose a modelling technique which allows us to incorporate frequency-dependent reflectivity into convolutional modelling. With this modelling framework, seismic data can be synthesized from well logs of velocity, density, porosity and water saturation. This forward modelling could act as a basis for inversion schemes aimed at recovering gas saturation variations with depth. We present a Bayesian inversion scheme for a simple thin layer case and a particular rock physics model, and show that although the method is very sensitive to prior information and constrains, gas saturation and layer thickness can both theoretically be estimated in the case of interfering reflections.

Keywords

Frequency-dependent AVO; Gas saturation; Seismic modelling; Rock physics; Thin layer

Introduction

Estimating gas saturation from seismic data is a fundamental problem in reservoir characterization (e.g. Batzle and Wang 1992; Avseth et al. 2005; Bachrach 2006; Chen et al. 2007). The importance of the problem for CO_2 monitoring has also become increasingly apparent in recent years (Xue and Ohsumi 2004; Carcione et al. 2006; Daley et al. 2008; Ivanova et al. 2012). Amplitude variation with offset (AVO) analysis from pre-stack seismic reflection data has been an important tool for fluid and lithology detection (Ostrander 1984; Rutherford and Williams 1989; Castagna and Backus 1993; Russell et al. 2003; Foster et al. 2010; Simm and Bacon 2014). During AVO analysis, Gassmann's equations (Gassmann 1951; Biot 1956) are often used to simulate changes in bulk and shear moduli from changing pore fluid. It is well known that the presence of gas in a reservoir often reduces P-wave velocity abruptly. However, in many cases only the first few percent of gas can be detected since further change of gas saturation brings small variations to P-wave velocity (Domenico 1976; González et al. 2003). This kind of velocity insensitivity is modelled by Gassmann's theory which predicts that bulk modulus is insensitive to gas saturation over a significant range. As a result, AVO often cannot be used to determine gas saturation.

Partial gas saturation is known to lead to seismic attenuation and dispersion (White 1975), and a vast literature exists on methods to accurately describe the phenomenon at different scales. This includes discussion of "bubble" effects (Dutta and Odé 1979; Carcione et al. 2003; Quintal et al. 2008; Rubino and Holliger 2012) as well as scale and frequency dependent transition between "patchy" and "uniform" saturation effects (Mavko and Mukerji 1998a; Lebedev et al. 2009; Müller et al. 2010). Laboratory measurements by Murphy (1982), Murphy (1984), Tisato and Quintal (2013), Amalokwu et al. (2014) and Tisato et al. (2015) also show that attenuation tends to be sensitive to partial gas saturation.

The relationship between bulk modulus and gas saturation can therefore be frequency dependent, which is not accounted for by Gassmann's theory. In principle, attenuation may be sensitive to gas saturation (Dasgupta and Clark 1998). However, the difficulty in measuring attenuation from seismic data and the uncertainty in the underlying rock physics have hindered the application of this technique (Dasgupta and Clark 1998; Reine et al. 2009).

Increasing attention has been paid to the potential for dispersion and attenuation to produce a frequency-dependent reflection coefficient. Dutta and Odé (1983) considered reflections from the interface between poroelastic materials saturated with water and gas, and predicted modest effects on the reflection coefficient at seismic frequencies. Their study was based on the Biot (1956) theory, which predicted small dispersion at seismic frequencies. Later work by Pride et al. (2004) showed how a sequence of saturated poroelastic layers can lead to significant dispersion effects. Since then, authors have analyzed similar problems using models which do show significant gas-related dispersion at seismic frequencies, and have concluded that frequency-dependent reflectivity could be potentially important (Chapman et al. 2006; Odebeatu et al. 2006; Ren et al. 2009; Innanen 2011). Wu et al. (2014) proposed a method for inverting pre-stack reflection data for gas saturation based on frequency-dependent reflectivity and rock physics theory. The method involves forward modelling of the reflection coefficient using frequency-dependent rock physics theories, applying spectral decomposition and balancing to seismic data to obtain the spectral amplitudes of reflection coefficients at varying angles of incidence, and making comparison between the observed data and model responses to perform a Bayesian inversion for water saturation. The technique was shown to have the potential of being able to differentiate full gas saturation, partial gas saturation and full water saturation under apparently reasonable assumptions.

Despite the progress from Wu et al. (2014), a number of limitations underlie the technique: there has to be only one interface in the reservoir and dispersion only occurs in the lower half

space as the upper layer is assumed to be elastic. A key weakness of the single-interface assumption is that the results from spectral decomposition can be corrupted by closely spaced interfering reflections from a thin layer in the circumstance where the reservoir consists of multiple layers. In this case, it is not likely to obtain an accurate estimation of gas saturation by using current Frequency-dependent AVO analysis.

In this paper, we address these limitations by investigating the possibility of recovering both gas saturation and thickness of a thin-layer reservoir. We develop an approach to calculating synthetic seismograms from well logs of P-wave velocity, S-wave velocity, density, porosity and water saturation. We show how this forward seismic model can act as a basis for a Bayesian inversion scheme that estimates gas saturation and layer thickness with suitable prior information. Our results from a thin layer study show that with sufficient prior geological knowledge, we can handle interfering reflections and the quantitative gas saturation estimation method by Wu et al. (2014) can be effectively extended to the thin-layer case.

We start from a brief review of the underlying physics theory we will use and then explain how the frequency-dependent reflection coefficient in partially saturated rocks is calculated from Zoeppritz equations generalized by Schoenberg and Protazio (1992). We then propose a generalized convolutional model for frequency-dependent reflectivity series, from which synthetic seismograms can be generated from well logs in multi-layer fluid saturated reservoir in time domain. The forward model can then be used to perform the Bayesian inversion for the recovery of water saturation and reservoir thickness. Finally, we demonstrate a numerical example, which is based on a thin layer model embedded between two half spaces, to show the potential application of this method.

Frequency-dependent rock physics theory

We base our study of frequency-dependent reflectivity on a poroelastic rock physics model by Chapman et al. (2002), which is a squirt-flow theory considering fluid exchange between pores and cracks, as well as between cracks of different orientations due to wave propagation. The model assumes an idealized microstructure consisting of thin cracks and spherical pores, and models velocity dispersion and attenuation arising due to wave-induced fluid flow. Chapman et al. (2002) gave expressions for the frequency-dependent bulk and shear moduli of a fluid saturated porous rock:

$$K_{eff}(\omega) = \lambda + \frac{2}{3}\mu - \frac{4}{3}\varepsilon\frac{\left(\lambda+\frac{2}{3}\mu\right)^2(\lambda+2\mu)}{\mu(\lambda+\mu)} - \phi\frac{\left(\lambda+\frac{2}{3}\mu\right)(\lambda+2\mu)}{4\mu} + \varepsilon\left[\frac{4\left(\lambda+\frac{2}{3}\mu\right)^2(\lambda+2\mu)}{3\mu(\lambda+\mu)} + 4\pi r\left(\lambda+\frac{2}{3}\mu\right)\right]A(\omega) + \phi\frac{9\left(\lambda+\frac{2}{3}\mu\right)(\lambda+2\mu)}{4\mu}B(\omega), \quad (1)$$

$$\mu_{eff}(\omega) = \mu - \frac{16}{45}\varepsilon\frac{1}{1+K_c}\frac{\mu(\lambda+2\mu)}{3\lambda+4\mu}\left(K_c + \frac{1}{1+i\omega\tau}\right) - \frac{32}{45}\varepsilon\frac{\mu(\lambda+2\mu)}{3\lambda+4\mu} - \phi\frac{15\mu(\lambda+2\mu)}{9\lambda+14\mu}, \quad (2)$$

where ω is the angular frequency, μ and λ are the shear modulus and the Lamé parameter of the non-porous matrix. ε is the crack density, r is the crack aspect ratio, ϕ is the total porosity, and τ is a timescale parameter that controls the frequency range of dispersion.

$A(\omega)$ and $B(\omega)$ are frequency-dependent constants defined by

$$A(\omega) = \frac{\frac{i\omega\tau}{3(1+K_c)} - \gamma' i\omega\tau + \frac{1}{\gamma}(1+i\omega\gamma\tau)\left[\frac{1}{3(1+K_c)} + \gamma'\right]}{1+i\omega\tau+\frac{1}{\gamma}(1+i\omega\gamma\tau)}, \quad (3)$$

$$B(\omega) = \frac{(1+i\omega\tau)\left[\frac{1}{3(1+K_c)} + \gamma'\right] - i\omega\tau\left[\frac{1}{3(1+K_c)} - \gamma'\right]}{1+i\omega\gamma\tau+\gamma(1+i\omega\tau)}, \quad (4)$$

where γ and γ' are non-dimensional parameters:

$$\gamma = \frac{9\phi(\lambda+\mu)(1+K_p)}{16\varepsilon(\lambda+2\mu)(1+K_c)}, \quad (5)$$

$$\gamma' = \gamma\frac{\lambda+2\mu}{(3\lambda+2\mu)(1+K_p)}. \quad (6)$$

K_c is called the crack-space compressibility parameter, and can be expressed as

$$K_c = \frac{\pi\mu(\lambda+\mu)r}{K_f(\lambda+2\mu)}, \quad (7)$$

where K_f is the fluid bulk modulus. Similarly, the pore-space compressibility parameter K_p is given by

$$K_p = \frac{4\mu}{3K_f}. \tag{8}$$

In the case where the reservoir is saturated by water and gas, K_f can be estimated by Wood's equation (Wood 1955)

$$K_f = \frac{1}{\frac{1-S_w}{K_g}+\frac{S_w}{K_w}}, \tag{9}$$

where S_w is water saturation, K_w and K_g are the bulk moduli of water and gas respectively. In this paper, K_w has the value of 2.0 GPa, and K_g is chosen to be 0.2 GPa.

The timescale parameter τ is proportional to fluid viscosity and inversely proportional to the permeability. That is to say, its reciprocal actually plays the role of fluid mobility, which is the ratio of permeability to fluid viscosity. Wu et al. (2014) has discussed the practical implementation of these equations by relating the effective bulk and shear moduli with reference P-wave velocity, S-wave velocity and density. We can then calculate the frequency-dependent reflectivity from Zoeppritz equations generalized by Schoenberg and Protazio (1992).

Reflectivity from materials exhibiting dispersion and attenuation

The exact calculation of the amplitudes of reflected and transmitted plane waves from both incident P- and S-waves at an interface between two elastic media is given by Zoeppritz equations (Zoeppritz 1919). The original form of Zoeppritz equations is too complicated to directly interpret the variation of reflection coefficient with rock properties. There have been some simplifications developed to better solve elastic problems (Aki and Richards 1980; Fatti et al. 1994; Shuey 1985; Smith and Gidlow 1987). The corresponding viscoelastic case has been studied by Borcherdt (2009).

Wu et al. (2014) calculated frequency-dependent reflectivity for an elastic layer overlying a dispersive and attenuative lower layer. The elastic behaviour of the upper layer allowed them to construct solutions in which the slowness vector in the upper medium was real, and only the vertical components of slowness in the lower layer were complex – a substantial simplification.

In this paper, we assume that the horizontal components of slowness are all real, which may correspond to flat layers and the source being placed in an elastic layer.

Assuming that the isotropic medium has a mirror plane of symmetry parallel to the $X_1 - X_2$ plane, let $X_3 = 0$ be the horizontal interface. When waves propagate in the vertical $X_1 - X_3$ plane, the displacement is given by

$$\mathbf{u} = \begin{bmatrix} e_1 \\ e_3 \end{bmatrix} \exp \mathrm{i}\omega(s_1 \mathrm{x}_1 + s_3 \mathrm{x}_3 - t), \tag{10}$$

where e_1 and e_3 represent polarizations, s_1 is horizontal slowness, and s_3 is vertical slowness. The wavefield in the upper medium includes incident and reflected P- and S-waves while the lower medium only has transmitted waves. The displacement field in the upper layer can be written as

$$\begin{bmatrix} v_1 \\ v_3 \end{bmatrix} = i_p \begin{bmatrix} e_{p1} \\ e_{p3} \end{bmatrix} \exp \mathrm{i}\omega s_{3_p} \mathrm{x}_3 + r_p \begin{bmatrix} e_{p1} \\ -e_{p3} \end{bmatrix} \exp -\mathrm{i}\omega s_{3_p} \mathrm{x}_3$$
$$+ i_s \begin{bmatrix} e_{s1} \\ e_{s3} \end{bmatrix} \exp \mathrm{i}\omega s_{3_s} \mathrm{x}_3 + r_s \begin{bmatrix} e_{s1} \\ -e_{s3} \end{bmatrix} \exp -\mathrm{i}\omega s_{3_s} \mathrm{x}_3, \tag{11}$$

where i_p, r_p, i_s, and r_s are amplitudes of the incident P-wave, reflected P-wave, incident S-wave and reflected S-wave respectively. s_{3_p}, s_{3_s}, e_{p1}, e_{p3}, e_{s1} and e_{s3} are vertical slowness and polarizations for P- and S-waves. ω is the frequency of the incident strain wave. In the case where there is only incident P-wave, we can set i_s to be zero.

The lower medium only has transmitted P- and S-waves, making the displacement field be given by

$$\begin{bmatrix} v_1{}' \\ v_3{}' \end{bmatrix} = t_p \begin{bmatrix} e_{p1}{}' \\ e_{p3}{}' \end{bmatrix} \exp \mathrm{i}\omega s_{3_p}{}' \mathrm{x}_3 + t_s \begin{bmatrix} e_{s1}{}' \\ e_{s3}{}' \end{bmatrix} \exp \mathrm{i}\omega s_{3_s}{}' \mathrm{x}_3, \tag{12}$$

where t_p and t_s are amplitudes of the transmitted P- and S-waves, and all the other primed parameters have the same meanings as the unprimed ones in equation (11).

It is clear that the key to calculating the reflection coefficient is to obtain the vertical slowness as well as the polarizations of the ray. We do this with the help of the Christoffel equation, which from a given horizontal slowness allows us to calculate the vertical slownesses and corresponding polarization vectors.

With both horizontal and vertical slowness, as well as the polarizations of the wave at frequency ω from each layer being achieved, Schoenberg and Protazio (1992) solved Zoeppritz equations by introducing two impedance matrices

$$\mathbf{X} = \begin{bmatrix} e_{p1} & e_{s1} \\ -(c_{1133}s_1 e_{p1} + c_{3333}s_{3_p} e_{p3}) & -(c_{1133}s_1 e_{s1} + c_{3333}s_{3_s} e_{s3}) \end{bmatrix},$$

$$\mathbf{Y} = \begin{bmatrix} -c_{1331}(s_1 e_{p3} + s_{3_p} e_{p1}) & -c_{1331}(s_1 e_{s3} + s_{3_s} e_{s1}) \\ e_{p3} & e_{s3} \end{bmatrix}, \tag{13}$$

where in our case c_{1133}, c_{3333} and c_{1331} are frequency-dependent elastic moduli of the stiffness tensor with bulk modulus $K_{eff}(\omega)$ and shear modulus $\mu_{eff}(\omega)$ determined from Chapman et al. (2002) squirt model.

Let the upper layer be characterized by impedance matrices $\mathbf{X}$ and $\mathbf{Y}$, as are shown in equation (13), and the lower layer be associated with $\mathbf{X}'$ and $\mathbf{Y}'$, which have the same form as equation (13) but with the elements being primed parameters, the frequency-dependent reflection matrix is calculated to be

$$\mathbf{R} = \left(\mathbf{Y}'^{-1}\mathbf{Y} + \mathbf{X}'^{-1}\mathbf{X}\right)^{-1}\left(\mathbf{Y}'^{-1}\mathbf{Y} - \mathbf{X}'^{-1}\mathbf{X}\right). \tag{14}$$

The P-to-P reflection coefficient at frequency ω is given by R_{11} from the solution of equation (14). In this case, the P-to-P reflection coefficient is frequency dependent and complex.

Numerical modelling

In our model, the effect of attenuation and velocity dispersion is illustrated in Figure 1, with the model parameters chosen from the lower layer in Table 1. The relationship between water saturation and attenuation is peaked with a maximum around 80% water saturation. In general, the level of water saturation leading to the highest attenuation is model dependent, but it usually occurs within the range of 50% to 90% in our modelling framework (Wu et al. 2014). With appropriate value of relaxation time, which functions as fluid mobility in the rock physics model, P- and S-wave velocities are seen to increase with frequency in the seismic range.

Figure 2a shows the amplitude of the frequency-dependent reflection coefficient varying with angle of incidence from the Class IV AVO model in Table 1. Figure 2b displays the corresponding phase variation, which is determined by the ratio of the real and imaginary parts of the complex reflection coefficient. A detailed interpretation of phase variation in dispersive medium has been presented by Wu et al. (2015).

Having studied the effect of velocity dispersion to seismic reflection from rock physics, we propose and implement a forward modelling strategy that calculates synthetic angle-domain seismic traces from dispersive media with multiple layers. The method assumes the availability of well logs of P-wave velocity, S-wave velocity, density, porosity and water saturation in the two-way time domain. As is known, conventional synthetic seismic traces can be generated by the convolution of seismic source with reflectivity time series. When seismic dispersion occurs, reflection coefficient becomes frequency dependent, making it difficult to apply convolution in time domain. Below we propose a solution to this problem.

We first sample the target reservoir into finite layers separated by different interfaces at time depth of t_0, t_1, t_2, … t_k, where k is the total number of interfaces.

We then define the unit reflectivity i_t at nth interface as

$$i_t^n = \delta(t - n\Delta t), \tag{15}$$

where t is the time depth, Δt is the sampling interval.

In a reservoir consisting of multiple layers, each interface along with the neighbouring fluid saturated media contributes to the calculation of frequency-dependent reflectivity series, which are distributed along the time depths of the interfaces.

For a certain angle of incidence θ, the forward model of frequency-dependent seismic trace is derived as

$$x_t(\theta) = \sum_{n=1}^{k} i_t^n * \mathcal{F}^{-1}[W(\omega) \cdot R^n(\theta, \omega)], \tag{16}$$

where $W(\omega)$ is the incident wavelet $w(t)$ in frequency domain, $R^n(\theta, \omega)$ is the frequency-dependent reflection coefficient at time depth t_n, $\cdot$ denotes multiplication, $\mathcal{F}^{-1}$ denotes the inverse Fourier transform, and $*$ denotes convolution.

The idea behind the derivation is to calculate the reflected waveforms at different time depths by multiplication of the source with complex reflection coefficient in the frequency domain before transforming them back to time domain and stacking all the corresponding waveforms to generate the full seismic trace. Attenuation and dispersion effects on transmission have been neglected during this derivation. Transmission effects are cumulative, and become important as the ray path through the attenuating layer increases. The potential impact of these transmission effects depends on the magnitude of the dispersion and the thickness of the transmitting layer. Chapman et al. (2006) and Odebeatu et al. (2006) have discussed the relative importance of these effects with reference to typical models.

Figure 3 illustrates the calculated synthetic zero-offset ($\theta = 0°$) seismic trace for the single-interface Class IV model. In this paper, we used a Ricker wavelet with peak frequency of 40 Hz as the source $w(t)$. Compared with the elastic case, where fluid-induced dispersion is not considered, the frequency-dependent waveform is reshaped and shifted due to velocity dispersion.

Since the frequency-dependent reflection coefficient $R^n(\theta, \omega)$ is directly related to parameters such as V_P, V_S, ρ, ϕ and S_w, our derived forward model has the ability to generate seismic traces from well logs of the target reservoirs that consist of multiple layers exhibiting velocity dispersion. Below we show examples of synthetic seismic traces by using a single layer model embedded between two half spaces in Table 2, of which the well logs are displayed in Figure 4. According to Rutherford and Williams (1989) and Castagna and Swan (1997), the first and second horizons of this model give Class I and Class IV AVO responses, respectively.

Figure 5 displays the pre-stack angle-domain seismic trace from well logs in Figure 4a, with the reservoir thickness being 94.5 meters. The vertical axis is the two-way time (TWT) of the profile, and the horizontal axis is the angle of incidence. In this case, our 40 Hz Ricker wavelet and P-wave velocity of 3150 m/s would correspond to a conventional tuning thickness of approximately 19.7 meters (Widess 1973).

In the frequency-independent case, which is illustrated in Figure 5a, polarity change has been observed in the recorded waveforms from the first horizon. As the angle increases, the amplitude of the waveform gradually reduces to zero, at which the polarity of reflection changes abruptly from positive to negative as the angle continues to increase. The seismic response from the second horizon obeys the characteristics of the Class IV AVO, where there is a continuous slight decrease in amplitude as the angle increases.

The introduction of dispersion and attenuation results in significant differences in the seismic traces. Figure 5b displays the frequency-dependent pre-stack seismic profile. Apart from the reshaped waveform, as described in Figure 3, the most significant difference lies in the behaviour with regard to polarity change. Firstly, the amplitude of reflected waveform never reduces to zero; Secondly, the frequency-dependent seismic trace from the first horizon is

seen to have a gradual variation in both amplitude and phase, which is in contrast to the abrupt polarity change from the elastic case.

In the circumstance where the reservoir thickness of the model in Table 2 is decreased to 31.5 m, interfering reflections occur. Figure 6 displays this thin layer effect calculated from well logs in Figure 4b.

By varying the reservoir thickness linearly from 94.5 m to 15.75 m, a wedged model in Figure 7 is used to better demonstrate the interfering reflections. The comparison between the zero-offset gathers shows small differences between the elastic and frequency-dependent cases. By changing the incidence to a certain angle, e.g. 20 degrees in Figures 7c and 7d, we can observe differences in terms of amplitude and phase variation between these two cases. The forward seismic modelling can therefore generate seismic profiles consisting of multiple dispersive or elastic layers with arbitrary thickness, and the effects of frequency-dependent reflectivity on the waveforms are visible on synthetic seismograms.

Bayesian inversion scheme for water saturation and reservoir thickness

Statistical inversion is a popular approach for inferring rock properties from seismic data (Mavko and Mukerji 1998b; Buland and Omre 2003; Spikes et al. 2007). Bachrach (2006) presented a Bayesian scheme for joint estimation of porosity and saturation. Our proposed approach is a Bayesian inversion of pre-stack seismic data to estimate water saturation S_w and reservoir thickness h in a thin layer model where all other parameters are considered to be known. We construct the thin layer model by embedding the partially saturated reservoir between two shale half spaces, which is enough to simulate the interfering reflections. The Bayesian inversion equation for this problem is given by

$$P(S_w, h|d) = \frac{P(d|S_w,h)P(S_w,h)}{P(d)}, \tag{17}$$

where $P(S_w, h)$ is the prior information of S_w and h, $P(d)$ is a constant given that the data has been acquired. $P(d|S_w, h)$ is the likelihood function that exponentially relates to the misfit between the model response at (S_w, h) and the observed data d. As long as all these terms are acquired, the posterior probability $P(S_w, h|d)$ can be solved.

The inversion scheme is as follows:

(i) We begin by considering that the confounding background parameters are known, which allows us to forward model the seismic trace $f(S_w, h)$, as is rewritten from equation (16), for various values of water saturation S_w and thickness h. In a real application, representative values or probability distributions for these parameters would have to be estimated from well log data.

(ii) The misfit ΔE is calculated by summarizing the L_2-norm of the difference between the observed data d and forward model response at (S_w, h):

$$\Delta E = \sum \|d - f(S_w, h)\|_2. \tag{18}$$

(iii) The likelihood function $P(d|S_w, h)$, which measures the probability of data d given that the hypothesis is (S_w, h), is calculated by

$$P(d|S_w, h) = a \cdot \exp(-b \cdot \Delta E), \tag{19}$$

where a is the normalizing coefficient, and b is a constant. Equation (19) is motivated by the analysis of Ulrych et al. (2001), Mavko and Mukerji (1998b) and Kirkpatrick et al. (1983). Ulrych et al. (2001) and Mavko and Mukerji (1998b) theoretically explain how the determination of b can be related to the standard errors of observations, while Kirkpatrick et al. (1983) interprets equation (19) as an empirical relationship. In this paper, we determine the value of b to be 30 for illustration purposes in the following synthetic example.

(iv) The prior information $P(S_w, h)$ can be derived from well-log analysis, assumption or seismic interpretation (Avseth et al. 2005). $P(d)$, the probability of data, is set to be a

constant that ensures the final probability distribution integrates to one along with the normalizing coefficient a from equation (19).

Finally, the posterior probability of inversion targets S_w and h of the reservoir under observed data d can be calculated by equation (17).

Synthetic example

Here we present a synthetic study by using model parameters in Table 3. Figure 8 shows the pre-stack observed data from reservoirs containing 20% and 80% water saturation, which are generated by adding 10% Gaussian noise to the synthetic traces calculated by equation (16).

We first derive the forward seismic model as a function of S_w and h from given confounding parameters in Table 3. We then scan through the combinations of S_w and h to calculate the misfits between observed data and model responses, from which the likelihood function $P(d|S_w, h)$ is transformed and displayed in Figure 9.

A uniform distribution of S_w is assumed given that there is no prior information on water saturation. A normal distribution $\mathrm{N}(30, 2.5)$ of h is assumed as the prior reservoir thickness. Figure 10 shows the corresponding prior probability distribution $P(S_w, h)$. The posterior probability $P(S_w, h|d)$ is therefore calculated by equation (17) by choosing appropriate value of $P(d)$ that normalizes the final probability distribution.

Figure 11 displays the posterior probability of S_w and h. For the 20% water case, the inverted h is about 30 m and S_w is around 20%. For the 80% water case, h is inverted to be 30 m and S_w is estimated to be 80%. The water saturations for both cases are accurately estimated, and it is clear that commercial gas is well distinguished from fizz water.

However, in practice, errors will always be present in the confounding parameters. As a result, the derived rock physics model may be different from the true one. Therefore, we introduced

errors to the well-log P-wave velocity as well as the rock physics parameter crack density, and repeated the inversion procedure to find out the impact of errors to the inversion quality. Figure 12 and Figure 13 show the posterior probability of S_w and h under different P-wave velocities. The actual velocity is 3.0 km/s, and we consider errors within a range of 0.1 km/s. In the case of 20% water saturation, the estimated S_w decreases as P-wave velocity increases. In contrast, when water saturation is 80%, the estimated S_w increases with P-wave velocity. Nevertheless, the 20% water saturation can still be clearly distinguished from the 80% one. Further expanding the errors to a wider range leads to unstable estimated results. It is noticed that for the 20% water case, as velocity increases, another local maximum posterior probability of S_w and h occurs and could result in a very high water saturation estimation. In this example, the inversion would break down when P-wave velocity is greater than 3.05 km/s, as is indicated by Figure 12f. The comparison between Figure 12 and Figure 13 indicates that differences still exist between the two cases since there is no such local maxima for the reservoir saturated by 80% water. Figure 14 shows the curves of the estimated S_w under varying P-wave velocities with errors within a range of 0.2 km/s. It is suggested from this example that the estimation provides reasonable results when the P-wave velocity errors are ± 0.05 km/s.

Figure 15 displays the likelihood function of S_w and P-wave velocity at fixed reservoir thickness of 30 meters. The results show that estimation of water saturation will potentially be more accurate if we can effectively constrain the layer thickness.

The impact of crack density turns out to be similar to that of P-wave velocity. In the case of 20% water saturation, Figure 16 shows that as crack density increases, two local maximum posterior probabilities of S_w and h can occur. The estimation of S_w can be inaccurate when crack density increases to 0.13 (true value is 0.1). In the case of 80% water saturation, Figure 17 shows that the estimation tends to have a more stable increasing trend as crack density

increases. The maximum probability curve in Figure 18 suggests that the estimation provides reliable results when crack density errors are less than around 20%.

Discussion

Studies of frequency-dependence on partially gas-saturated rock have been performed for many years, with Dutta and Odé (1979) being an important reference. Recently, Wu et al. (2014) has studied the potential use of frequency-dependent AVO analysis for the estimation of gas saturation from partially saturated reservoir. However, one of the key weaknesses of their technique is failing to handle interfering reflections in a thin layer. We address this problem by developing an efficient multi-layer frequency-dependent AVO modelling scheme that calculates synthetic seismic traces from well logs of velocity, density, porosity and water saturation. Instead of spectrally decomposing seismic data, which leads to corrupted results under interfering reflections, we perform the inversion by directly focusing on seismic waveforms simulated by the derived forward modelling. Our results suggest that the technique by Wu et al. (2014) can, at least in theory, be extended to a wider application.

Our paper is not meant to imply that we believe the forward problem of predicting dispersion and attenuation from the saturation is solved; it is not. We have based our calculations on only one model and, while we believe that many alternative models would give similar results, the applicability of this or any model is open to debate. Of course, the forward modelling could be repeated with a range of other models which consider different mechanisms. However, we do believe that application of the modelling framework we propose, in which seismic data can be synthesized from the saturation logs, could provide a novel test of the underlying theories and proposed dispersion mechanisms. If our approach does not match seismic data better than conventional convolution modelling then it may be rejected.

It is well known that single interface reflection coefficient based models can be unrealistic, and the thin layer model we used for our inversion is open to the same criticism. Our forward modelling scheme accepts full velocity, density, porosity and saturation well logs, so we could attempt to recover all these values as a function of depth through inversion. This is an important problem which we will address in future. The current inversion scheme, in combination with that of Wu et al. (2014), is offered simply as a minimal set of assumptions which will allow us to begin the process of setting up blind tests for the prediction of saturation from field data. Judgement on the applicability of the techniques must await the results of such field tests.

Our study generalizes convolutional modelling and so neglects lateral heterogeneity. This approach is fast enough to allow us to perform inversion, but in particular cases it may be advantageous to compare to finite difference modelling – particularly when the reservoir thickness is such that effects of attenuation and dispersion on transmission become important.

Recognition of the impacts of dispersion and attenuation in seismic data has implications beyond improved rock and fluid identification. In particular, we believe that the offset-dependent phase variations may have implications for application of seismic velocity analysis as there may be an ambiguity between moveout and phase.

In our numerical example, we only considered the simple thin layer case, which is a single layer model embedded between two half spaces. In practice, some cases will require a more complex starting model. Future research will focus on creating appropriate regularization strategies for such cases. For the rock physics model used in this paper, the relationship between velocity and gas saturation is controlled by the timescale parameter τ and crack density ε. When it comes to field data, successful application would depend on calibrating these parameters from the available well, as discussed by Wu et al. (2014).

Conclusion

We have proposed a method to incorporate frequency-dependent reflectivity into convolutional modelling. The method allows us to compute synthetic seismic traces from well logs of velocity, density, porosity and water saturation. Comparison with elastic modelling indicates that effects of the frequency-dependent reflectivity on the waveforms are visible on the synthetic seismograms for simple models based on sand-shale sequences. Such modelling provides a possible basis for inversion of gas saturation, and we tested the feasibility of such inversions using a simplified thin layer model and a Bayesian inversion scheme. The results indicated that, although the method is very sensitive to prior information and constrains, gas saturation and layer thickness can both theoretically be estimated in the case of interfering reflections.

Acknowledgements

MC and XW would like to thank the sponsors of the Edinburgh Anisotropy Project (EAP), British Geological Survey for financial support. GP's contribution to this work was carried out within the DiSECCS project https://www.bgs.ac.uk/diseccs. DiSECCS is funded by the Engineering and Physical Sciences Research Council (EPSRC) UK. We thank the anonymous reviewers for constructive suggestions that improved the manuscript.

References

Aki K. and Richards P.G. 1980. Quantitative Seismology, W.H. Freeman and Co.

Amalokwu K., Best A. I., Sothcott J., Chapman M., Minshull T. and Li X. Y. 2014. Water saturation effects on elastic wave attenuation in porous rocks with aligned fractures. Geophysical Journal International, ggu076.

Avseth P., Mukerji T. and Mavko G. 2005. Quantitative seismic interpretation: Applying rock physics tools to reduce interpretation risk. Cambridge University Press.

Bachrach R. 2006. Joint estimation of porosity and saturation using stochastic rock-physics modeling. Geophysics 71(5), O53-O63.

Batzle M. and Wang Z. 1992. Seismic properties of pore fluids. Geophysics 57(11), 1396-1408.

Biot M. A. 1956. Theory of propagation of elastic waves in fluidsaturated porous solid, I. Low frequency range, II. Higher frequency range. Journal of the Acoustical Society of America 28, 168–191.

Borcherdt R. D. 2009. Viscoelastic waves in layered media. Cambridge University Press.

Buland A. and Omre H. 2003. Bayesian linearized AVO inversion. Geophysics 68(1), 185-198.

Carcione J. M., Helle H. B. and Pham N. H. 2003. White's model for wave propagation in partially saturated rocks: Comparison with poroelastic numerical experiments. Geophysics 68(4), 1389-1398.

Carcione J. M., Picotti S., Gei D. and Rossi G. 2006. Physics and seismic modeling for monitoring CO2 storage. Pure and Applied Geophysics 163(1), 175-207.

Castagna J. P. and Backus M. M. 1993. AVO analysis-tutorial and review. Offset-dependent reflectivity: theory and practice of AVO analysis, 3-36.

Castagna J. P. and Swan H. W. 1997. Principles of AVO crossplotting. The leading edge 16(4), 337-344.

Chapman M., Liu E. and Li X.-Y. 2006. The influence of fluid sensitive dispersion and attenuation on AVO analysis. Geophysical Journal International 167, 89–105.

Chapman M., Zatsepin S. V. and Crampin S. 2002. Derivation of a microstructural poroelastic model. Geophysical Journal International 151, 427-451.

Chen J., Hoversten G. M., Vasco D., Rubin Y. and Hou Z. 2007. A Bayesian model for gas saturation estimation using marine seismic AVA and CSEM data. Geophysics 72(2), WA85-WA95.

Daley T. M., Myer L. R., Peterson J. E., Majer E. L. and Hoversten G. M. 2008. Time-lapse crosswell seismic and VSP monitoring of injected CO2 in a brine aquifer. Environmental Geology 54(8), 1657-1665.

Dasgupta R. and Clark R. A. 1998. Estimation of Q from surface seismic reflection data. Geophysics 63(6), 2120-2128.

Domenico S. N. 1976. Effect of brine-gas mixture on velocity in an unconsolidated sand reservoir. Geophysics 41(5), 882-894.

Dutta N. C. and Odé H. 1979. Attenuation and dispersion of compressional waves in fluid-filled porous rocks with partial gas saturation (White model)-Part I: Biot theory. Geophysics 44(11), 1777-1788.

Dutta N. C. and Odé H. 1983. Seismic reflections from a gas-water contact. Geophysics 48(2), 148-162.

Fatti J., Smith G., Vail P., Strauss P. and Levitt P. 1994. Detection of gas in sandstone reservoirs using AVO analysis: a 3D Seismic Case History Using the Geostack Technique. Geophysics 59, 1362-1376.

Foster D. J., Keys R. G. and Lane F. D. 2010. Interpretation of AVO anomalies. Geophysics 75(5), 75A3-75A13.

Gassmann F. 1951. Über die Elastizität poröserMedien: Vierteljahrsschrift der Naturforschenden Gesellschaft in Zürich, Vol. 96, 1–23.

González E. F., Mukerji T., Mavko G. and Michelena R. J. 2003. Near and far offset P-to-S elastic impedance for discriminating fizz water from commercial gas. The Leading Edge 22(10), 1012-1015.

Innanen K. A. 2011. Inversion of the seismic AVF/AVA signatures of highly attenuative targets. Geophysics 76(1), R1-R14.

Ivanova A., Kashubin A., Juhojuntti N., Kummerow J., Henninges J., Juhlin C., Lüth S. and Ivandic M. 2012. Monitoring and volumetric estimation of injected CO2 using 4D seismic, petrophysical data, core measurements and well logging: a case study at Ketzin, Germany. Geophysical Prospecting 60(5), 957-973.

Kirkpatrick S., Gelatt C. D. and Vecchi M. P. 1983. Optimization by simulated annealing. Science 220, 671-680.

Lebedev M., Toms-Stewart J., Clennell B., Pervukhina M., Shulakova V., Paterson L., Müller T. M., Gurevich B. and Wenzlau F. 2009. Direct laboratory observation of patchy saturation and its effects on ultrasonic velocities. The Leading Edge 28(1), 24-27.

Mavko G. and Mukerji T. 1998a. Bounds on low-frequency seismic velocities in partially saturated rocks. Geophysics 63(3), 918-924.

Mavko G. and Mukerji T. 1998b. A rock physics strategy for quantifying uncertainty in common hydrocarbon indicators. Geophysics 63(6), 1997-2008.

Müller T. M., Gurevich B. and Lebedev M. 2010. Seismic wave attenuation and dispersion resulting from wave-induced flow in porous rocks — A review. Geophysics 75(5), 75A147-75A164.

Murphy W. F. 1982. Effects of partial water saturation on attenuation in Massilon sandstone and Vycor porous glass. The Journal of the Acoustical Society of America 71, 1458-1468.

Murphy W. F. 1984. Acoustic measures of partial gas saturation in tight sandstones. Journal of Geophysical Research: Solid Earth 89, 11549-11559.

Odebeatu E., Zhang J., Chapman M., Liu E. and Li X.-Y. 2006. Application of spectral decomposition to detection of dispersion anomalies associated with gas saturation. The Leading Edge 25(2), 206-210.

Ostrander W. 1984. Plane-wave reflection coefficients for gas sands at nonnormal angles of incidence. Geophysics 49(10), 1637-1648.

Pride S. R., Berryman J. G. and Harris J. M. 2004. Seismic attenuation due to wave-induced flow. Journal of Geophysical Research: Solid Earth, 109(B1).

Quintal B., Schmalholz S. M. and Podladchikov Y. Y. 2008. Low-frequency reflections from a thin layer with high attenuation caused by interlayer flow. Geophysics 74(1), N15-N23.

Reine C., van der Baan M. and Clark R. 2009. The robustness of seismic attenuation measurements using fixed- and variable-window time-frequency transforms. Geophysics 74(2), WA123-WA135.

Ren H., Goloshubin G. and Hilterman F. 2009. Poroelastic analysis of amplitude-versus-frequency variations. Geophysics 74(6), N41-N48.

Rubino J. G. and Holliger K. 2012. Seismic attenuation and velocity dispersion in heterogeneous partially saturated porous rocks. Geophysical Journal International 188(3), 1088-1102.

Russell B. H., Hedlin K., Hilterman F. J. and Lines L. R. 2003. Fluid-property discrimination with AVO: A Biot-Gassmann perspective. Geophysics 68(1), 29-39.

Rutherford S. R. and Williams R. H. 1989. Amplitude-versus-offset variations in gas sands. Geophysics 54(6), 680-688.

Schoenberg M. and Protazio J. 1992. ‘Zoeppritz’ rationalized and generalized to anisotropy. Journal of Seismic Exploration 1, 125-144.

Shuey R. T. 1985. A simplification of the Zoeppritz equations, Geophysics 50, 609–614.

Simm R. and Bacon M. 2014. Seismic Amplitude: An interpreter's handbook. Cambridge University Press.

Smith G. C. and Gidlow P. M. 1987. Weighted stacking for rock property estimation and detection of gas, Geophysical Prospecting 35, 993–1014.

Spikes K., Mukerji T., Dvorkin J. and Mavko G. 2007. Probabilistic seismic inversion based on rock-physics models. Geophysics 72(5), R87-R97.

Tisato N. and Quintal B. 2013. Measurements of seismic attenuation and transient fluid pressure in partially saturated Berea sandstone: evidence of fluid flow on the mesoscopic scale. Geophysical Journal International, ggt259.

Tisato N., Quintal B., Chapman S., Podladchikov Y. and Burg J. P. 2015. Bubbles attenuate elastic waves at seismic frequencies: first experimental evidence. Geophysical Research Letters.

Ulrych T. J., Sacchi M. D. and Woodbury A. 2001. A Bayes tour of inversion: A tutorial. Geophysics 66(1), 55-69.

White J. E. 1975. Computed seismic speeds and attenuation in rocks with partial gas saturation. Geophysics 40(2), 224-232.

Widess M. B. 1973. How thin is a thin bed?. Geophysics 38(6), 1176-1180.

Wood A.W. 1955. A Textbook of Sound, Mcmillan Co.

Wu X., Chapman M., Li X.-Y. and Boston P. 2014. Quantitative gas saturation estimation by frequency-dependent Amplitude-Versus-Offset analysis. Geophysical Prospecting 62(6), 1224-1237.

Wu X., Chapman M. and Angerer E. 2015. Interpretation of phase reversals in seismic reflections from attenuating targets. Geophysical Journal International 200(1), 690-697.

Xue Z. and Ohsumi T. 2004. Seismic wave monitoring of CO2 migration in water-saturated porous sandstone. Exploration Geophysics 35(1), 25-32.

Zoeppritz K. 1919. Erdbebenwellen VIIIB, On the reflection and propagation of seismic waves: Göttinger Nachrichten I, 66-84.

Figure captions

Figure 1. Attenuation and velocity dispersion for the lower layer in Table 1. (a) P-wave and S-wave attenuation (1/Q) variation with frequency. (b) P-wave attenuation (1/Q) versus water saturation. (c) P-wave velocity dispersion. (d) S-wave velocity dispersion.

Figure 2. Reflection coefficients at the interface for the Class IV AVO model in Table 1. (a) Amplitude of the frequency-dependent reflection coefficient versus angle of incidence. (b) The corresponding phase of reflection coefficient versus angle of incidence.

Figure 3. Synthetic zero-offset trace for the Class IV AVO model in Table 1. The amplitude is rescaled to 1. The horizontal red line indicates the interface. The vertical red line is the reference for comparison of the waveforms. In the elastic case, where dispersion is not introduced, the waveform is in accord with the source Ricker wavelet. In the frequency-dependent case, the waveform is reduced in the upper layer and is amplified in the lower layer. The location of the peak is also shifted due to phase variation at different frequencies.

Figure 4. Well logs of P-wave velocity, S-wave velocity, density, porosity and water saturation for the model in Table 2. (a) Reservoir thickness is 94.5 m. (b) Reservoir thickness is 31.5 m.

Figure 5, Pre-stack angle-domain seismic gather for the laminated model in Table 2, with the reservoir thickness being 94.5 m. (a) Frequency-independent case. (b) Frequency-dependent case.

Figure 6, Pre-stack angle-domain seismic gather for the laminated model in Table 2, with the reservoir thickness being 31.5 m. (a) Frequency-independent case. (b) Frequency-dependent case.

Figure 7. Seismic gather for the wedge model in Table 2, with reservoir thickness varying from 15.75 m to 94.5 m. (a) Zero-offset frequency-independent case. (b) Zero-offset frequency-dependent case. (c) 20-degree frequency-independent case. (d) 20-degree frequency-dependent case.

Figure 8. Pre-stack seismic traces from reservoirs containing (a) 20% water saturation and (b) 80% water saturation. Model parameters are listed in Table 3. 10% Gaussian noise is added to synthetic traces calculated by equation (16) as the observed data.

Figure 9. Likelihood functions of reservoir thickness h and water saturation S_w for (a) 20% water case and (b) 80% water case. The true value of h (30m) and S_w (20% / 80%) is marked with white circle.

Figure 10. Prior information of reservoir thickness h and water saturation S_w. h is assumed to be normally distributed with mean value of 30 m and variation of 2.5; S_w is assumed to be uniformly distributed.

Figure 11. Posterior probability of reservoir thickness h and water saturation S_w for (a) 20% water case and (b) 80% water case. The true value of h (30m) and S_w (20% / 80%) is marked with white circle.

Figure 12. Posterior probability of h and S_w at varying well-log P-wave velocities for the reservoir saturated by 20% water. The true value of h (30m) and S_w (20%) is marked with white circle.

Figure 13. Posterior probability of h and S_w at varying well-log P-wave velocities for the reservoir saturated by 80% water. The true value of h (30m) and S_w (80%) is marked with white circle.

Figure 14. S_w with maximum posterior probability versus varying well-log P-wave velocities. The 20% water saturation case is indicated by blue circle, and the 80% water saturation case is labelled with red triangle. The true P-wave velocity is 3 km/s.

Figure 15. The likelihood function of water saturation S_w and P-wave velocity at fixed reservoir thickness of 30 meters. (a) 20% water case. (b) 80% water case.

Figure 16. Posterior probability of h and S_w at varying rock physics parameter crack densities ε for the reservoir saturated by 20% water. The true value of h (30m) and S_w (20%) is marked with white circle.

Figure 17. Posterior probability of h and S_w at varying rock physics parameter crack densities ε for the reservoir saturated by 80% water. The true value of h (30m) and S_w (80%) is marked with white circle.

Figure 18. S_w with maximum posterior probability versus varying crack densities. The 20% water saturation case is indicated by blue circle, and the 80% water saturation case is labelled with red triangle. The true crack density is 0.1.

Table 1. Parameters for a water & gas saturated single-interface Class IV AVO model

Layers	Vp (km/s)	Vs (km/s)	Density (g/cm^3)	Thickness (s)	Crack density	Porosity	Sw
Upper	3.200	1.620	2.49	0.03	0.1	0.3	10%
Lower	3.100	1.450	2.29	half space	0.1	0.3	90%

$K_g = 0.2\ GPa;\ K_w = 2.0\ GPa$

Table 2. Parameters for a water & gas saturated model

Layers	Vp (km/s)	Vs (km/s)	Density (g/cm^3)	Thickness (s)	Crack density	Porosity	Sw
Top	3.100	1.400	2.30	0.05	0.1	0.16	90%
Reservoir	3.150	1.600	2.50	(a) 0.06 (b) 0.02	0.1	0.2	10%
Bottom	3.060	1.580	2.33	half space	0.1	0.15	100%

$K_g = 0.2\ GPa;\ K_w = 2.0\ GPa$

Table 3. Parameters for a water & gas saturated thin layer model (the synthetic example)

Layers	Vp (km/s)	Vs (km/s)	Density (g/cm^3)	Thickness (s)	Crack density	Porosity	Sw
Top shale	3.200	1.500	2.40	0.04			
Reservoir	3.000	1.600	2.30	0.02	0.1	0.16	(a) 20% (b) 80%
Bottom shale	3.180	1.520	2.36	half space			

$K_g = 0.2\ GPa;\ K_w = 2.0\ GPa$

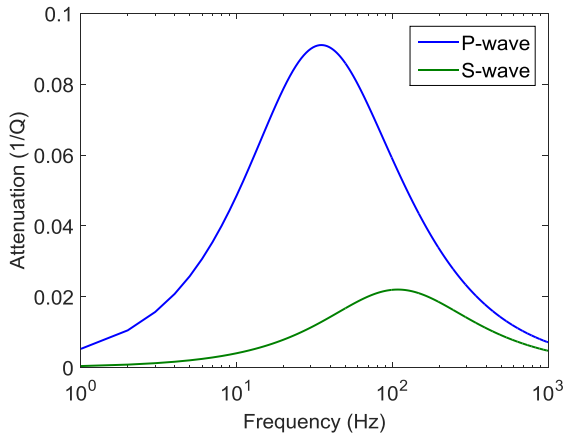

(a)

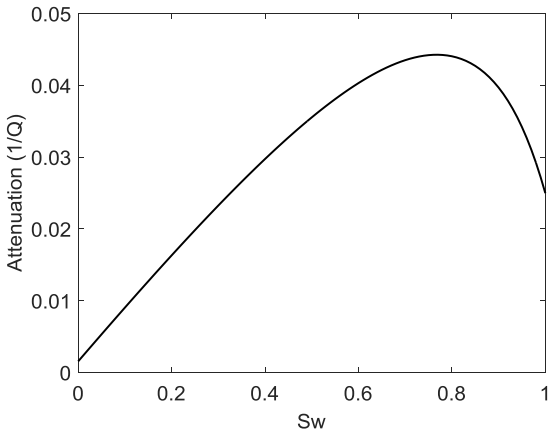

(b)

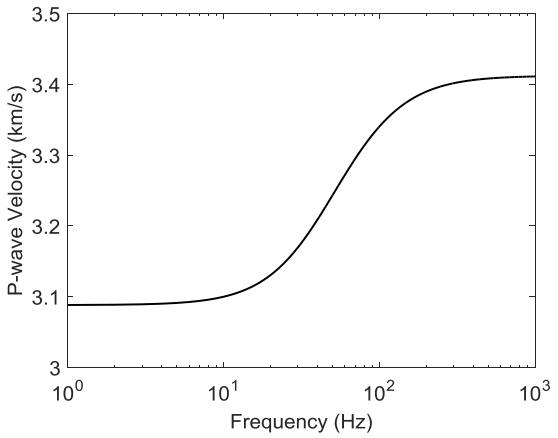

(c)

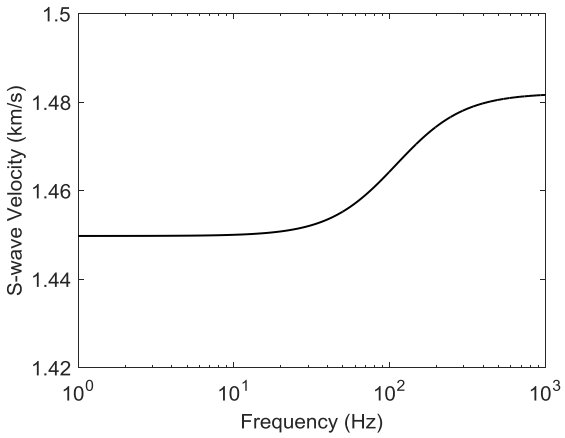

(d)

Figure 1. Attenuation and velocity dispersion for the lower layer in Table 1. (a) P-wave and S-wave attenuation (1/Q) variation with frequency. (b) P-wave attenuation (1/Q) versus water saturation. (c) P-wave velocity dispersion. (d) S-wave velocity dispersion.

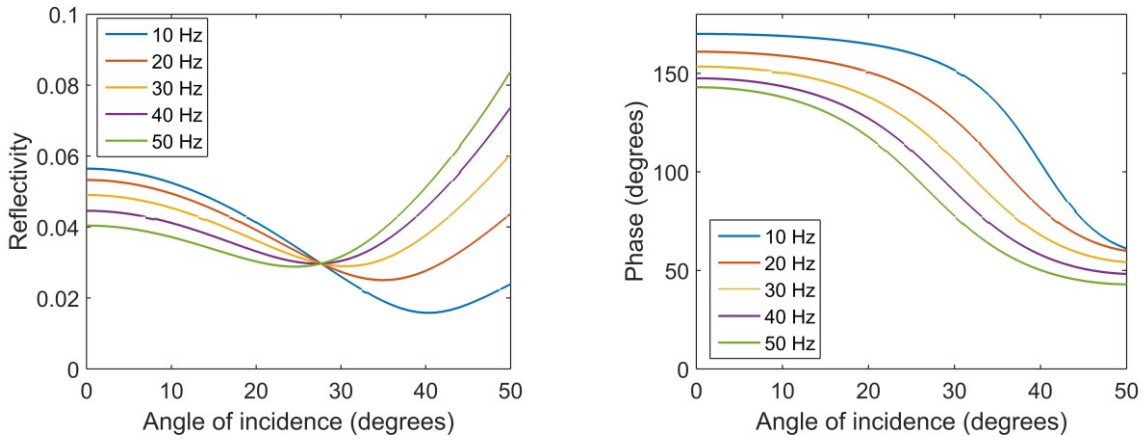

(a) (b)

Figure 2. Reflection coefficients at the interface for the Class IV AVO model in Table 1. (a) Amplitude of the frequency-dependent reflection coefficient versus angle of incidence. (b) The corresponding phase of reflection coefficient versus angle of incidence.

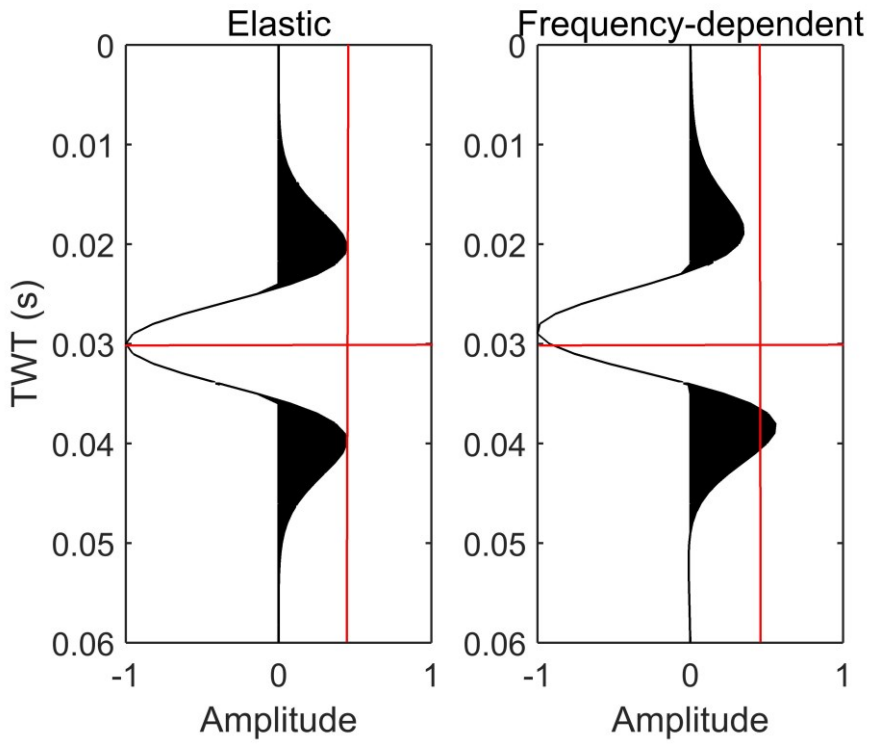

Figure 3. Synthetic zero-offset trace for the Class IV AVO model in Table 1. The amplitude is rescaled to 1. The horizontal red line indicates the interface. The vertical red line is the reference for comparison of the waveforms. In the elastic case, where dispersion is not introduced, the waveform is in accord with the source Ricker wavelet. In the frequency-dependent case, the waveform is reduced in the upper layer and is amplified in the lower layer. The location of the peak is also shifted due to phase variation at different frequencies.

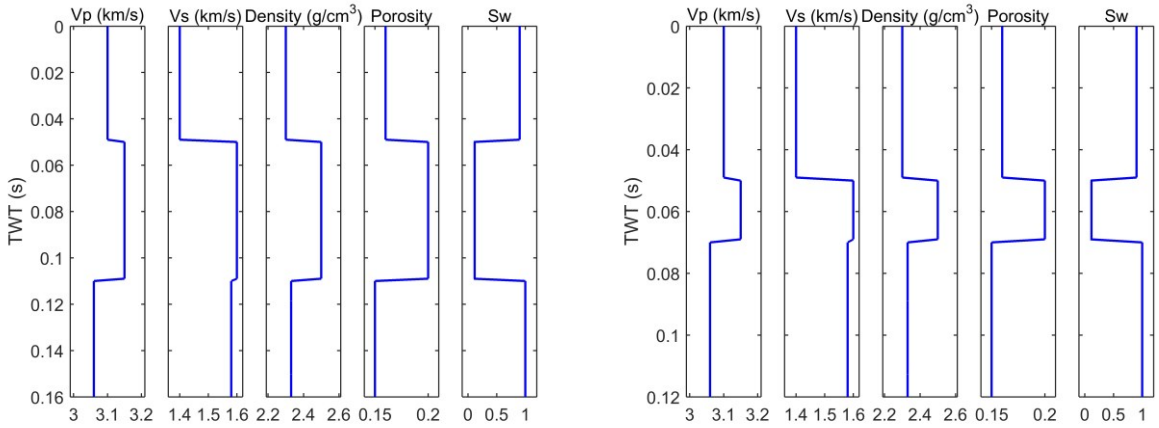

Figure 4. Well logs of P-wave velocity, S-wave velocity, density, porosity and water saturation for the model in Table 2. (a) Reservoir thickness is 94.5 m. (b) Reservoir thickness is 31.5 m.

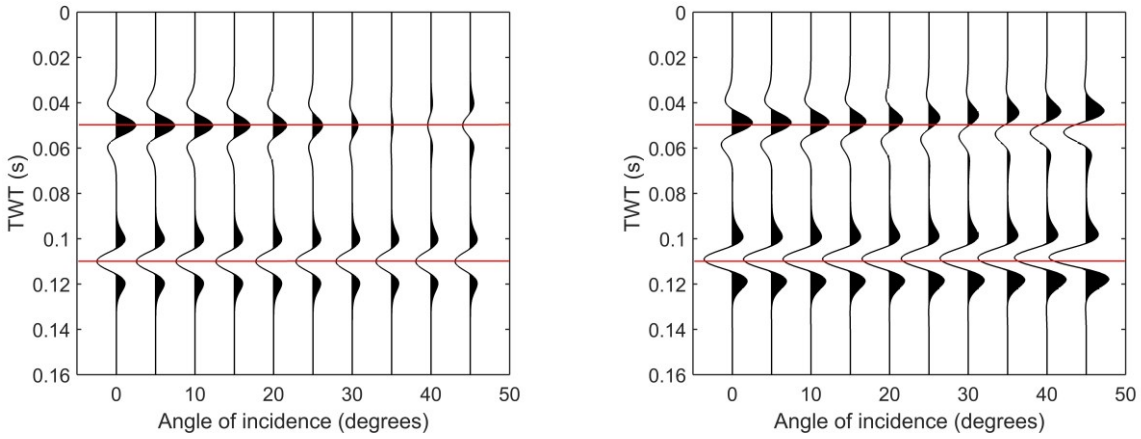

(a) (b)

Figure 5. Pre-stack angle-domain seismic gather for the laminated model in Table 2, with the reservoir thickness being 94.5 m. (a) Frequency-independent case. (b) Frequency-dependent case.

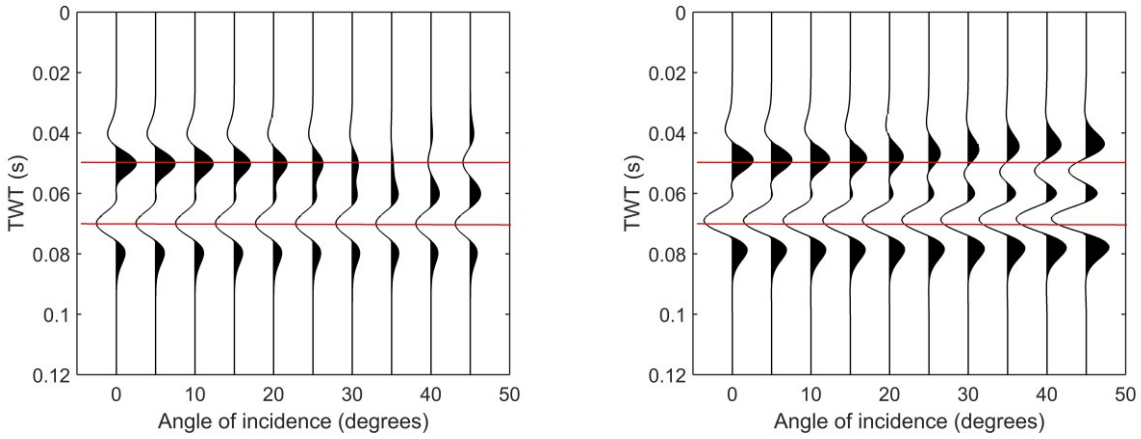

(a) (b)

Figure 6. Pre-stack angle-domain seismic gather for the laminated model in Table 2, with the reservoir thickness being 31.5 m. (a) Frequency-independent case. (b) Frequency-dependent case.

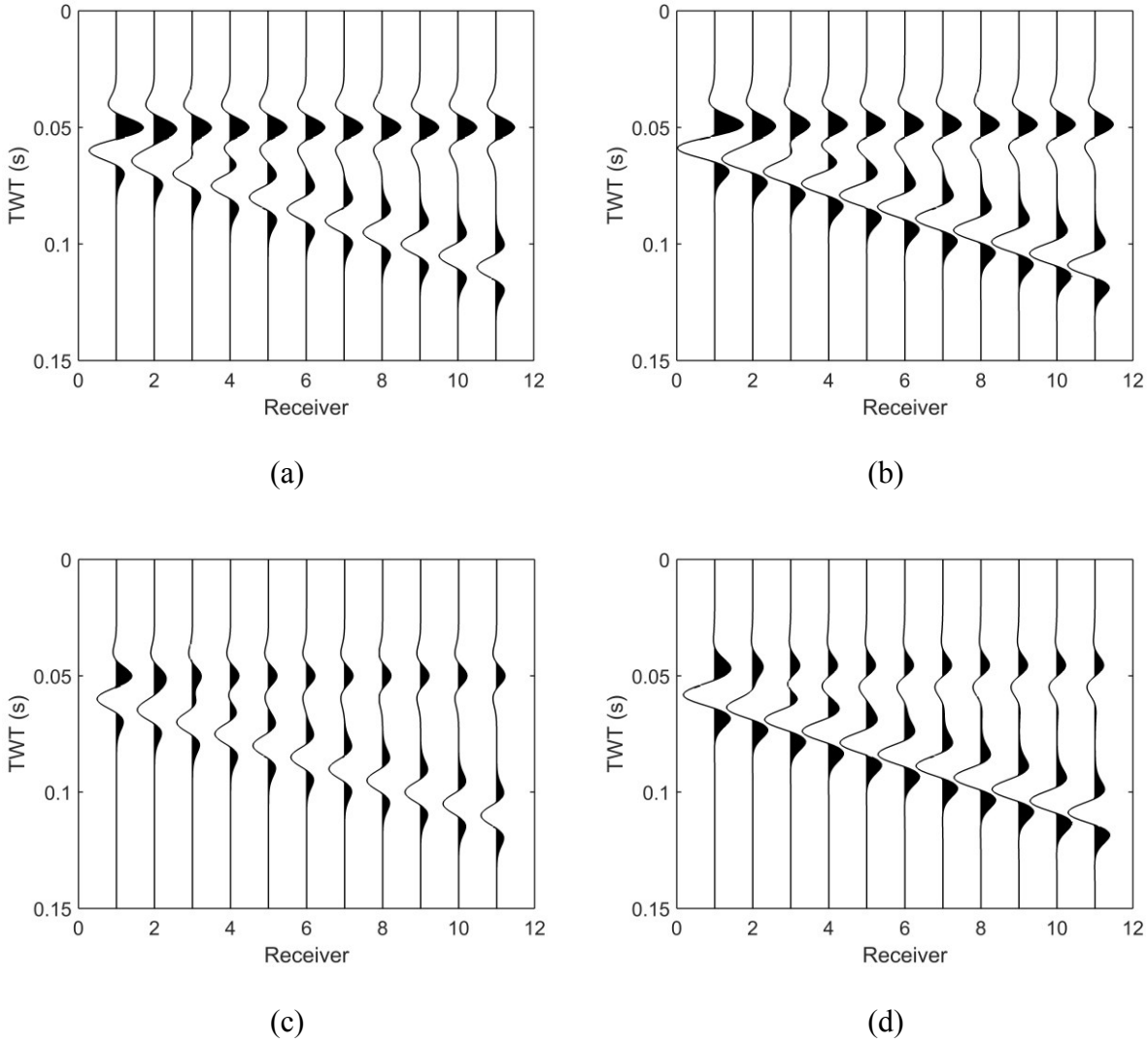

Figure 7. Seismic gather for the wedge model in Table 2, with reservoir thickness varying from 15.75 m to 94.5 m. (a) Zero-offset frequency-independent case. (b) Zero-offset frequency-dependent case. (c) 20-degree frequency-independent case. (d) 20-degree frequency-dependent case.

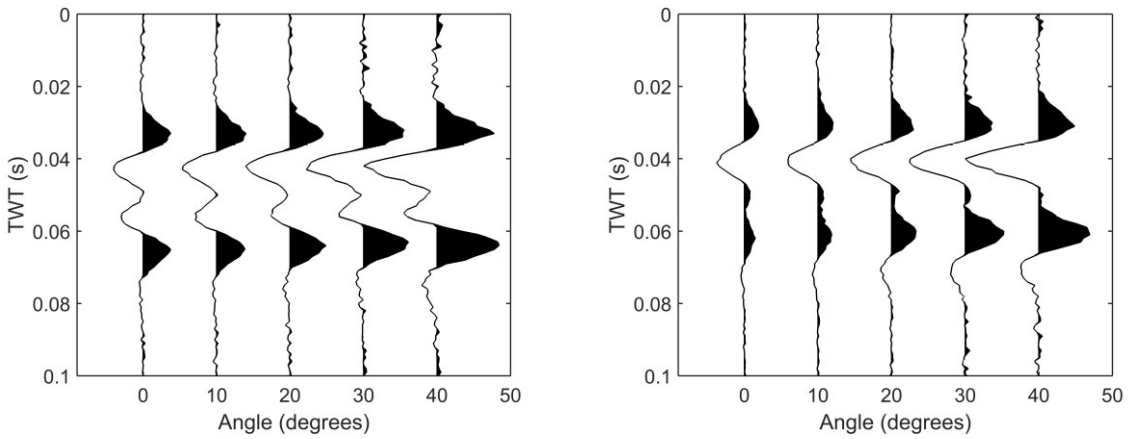

(a) Sw=20%

(b) Sw=80%

Figure 8. Pre-stack seismic traces from reservoirs containing (a) 20% water saturation and (b) 80% water saturation. Model parameters are listed in Table 3. 10% Gaussian noise is added to synthetic traces calculated by equation (16) as the observed data.

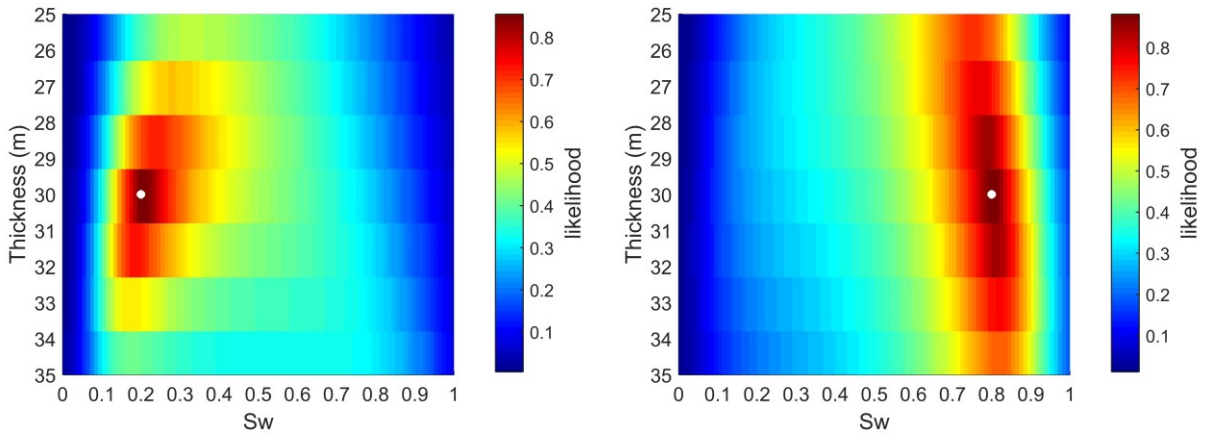

(a) Sw=20%

(b) Sw=80%

Figure 9. Likelihood functions of reservoir thickness h and water saturation S_w for (a) 20% water case and (b) 80% water case. The true value of h (30m) and S_w (20% / 80%) is marked with white circle.

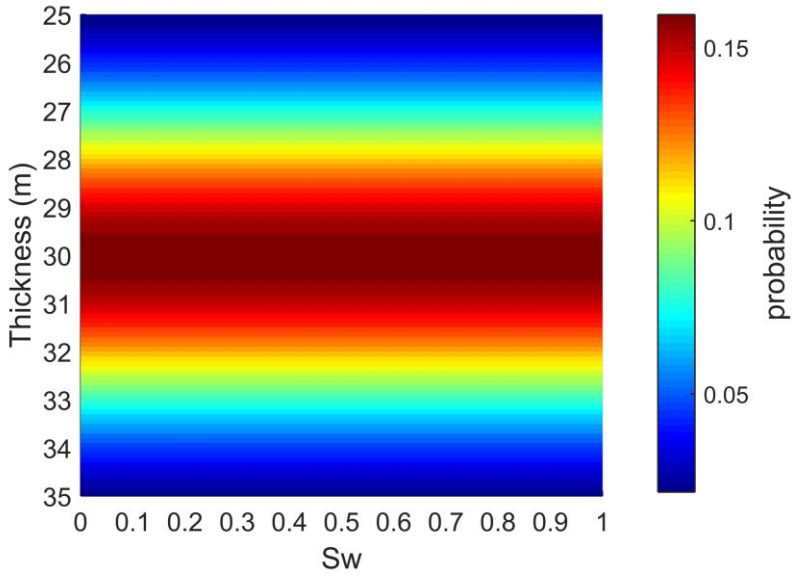

Figure 10. Prior information of reservoir thickness h and water saturation S_w. h is assumed to be normally distributed with mean value of 30 m and variation of 2.5; S_w is assumed to be uniformly distributed.

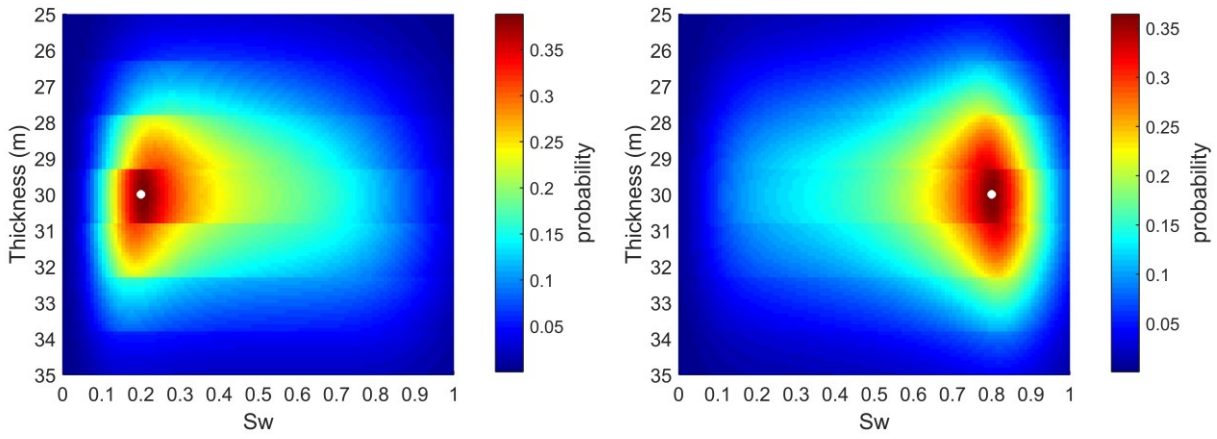

(a) Sw=20% (b) Sw=80%

Figure 11. Posterior probability of reservoir thickness h and water saturation S_w for (a) 20% water case and (b) 80% water case. The true value of h (30m) and S_w (20% / 80%) is marked with white circle.

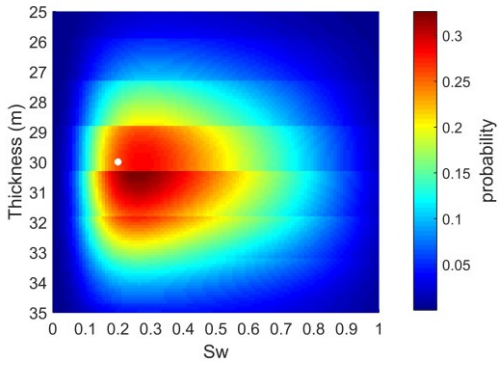

(a) Sw=20% Vp=2.95 km/s

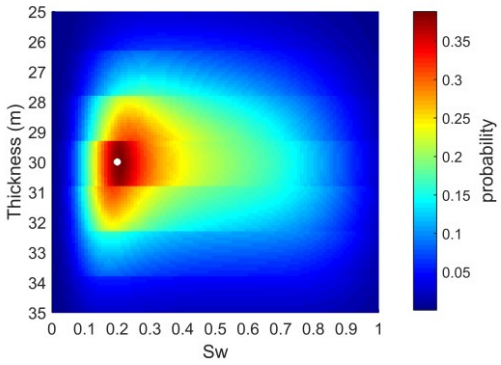

(b) Sw=20% Vp=3.00 km/s

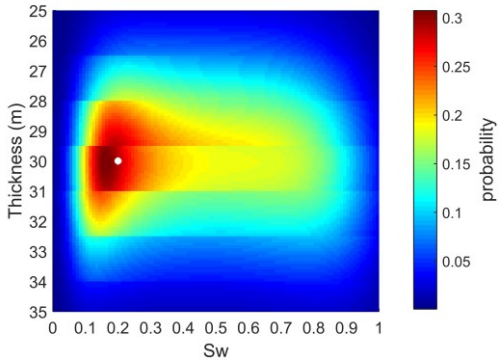

(c) Sw=20% Vp=3.02 km/s

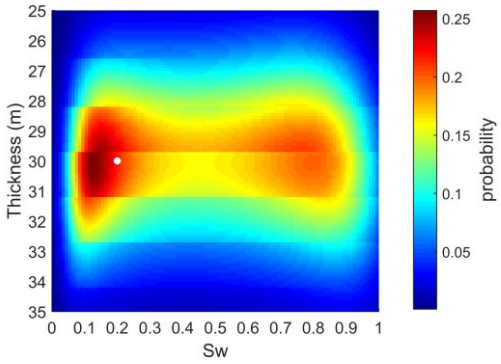

(d) Sw=20% Vp=3.04 km/s

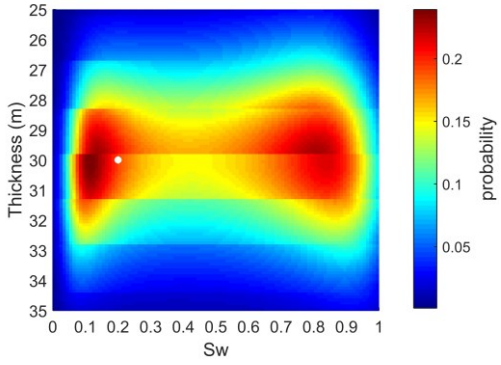

(e) Sw=20% Vp=3.05 km/s

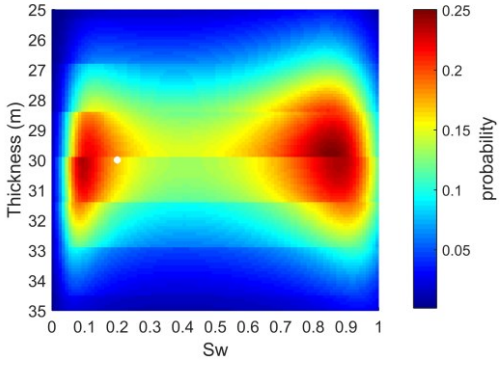

(f) Sw=20% Vp=3.06 km/s

Figure 12. Posterior probability of h and S_w at varying well-log P-wave velocities for the reservoir saturated by 20% water. The true value of h (30m) and S_w (20%) is marked with white circle.

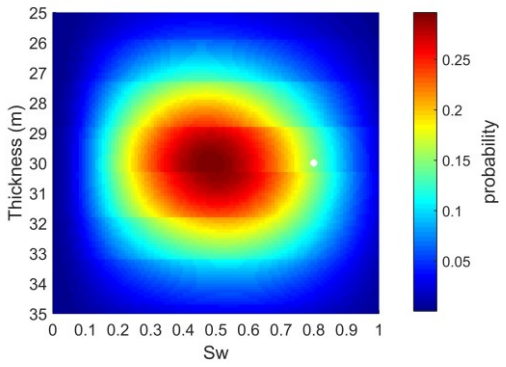

(a) Sw=80% Vp=2.95 km/s

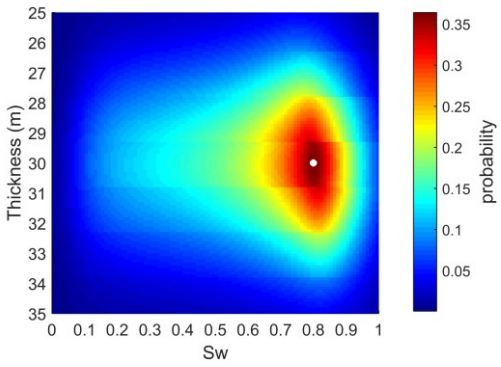

(b) Sw=80% Vp=3.00 km/s

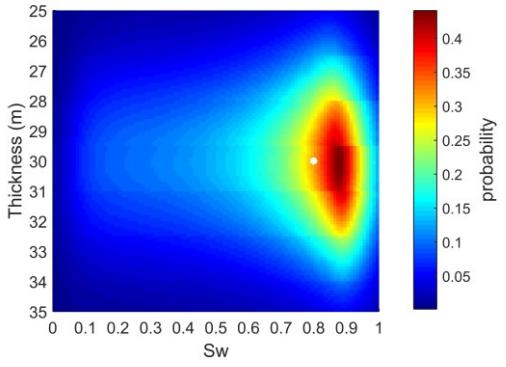

(c) Sw=80% Vp=3.02 km/s

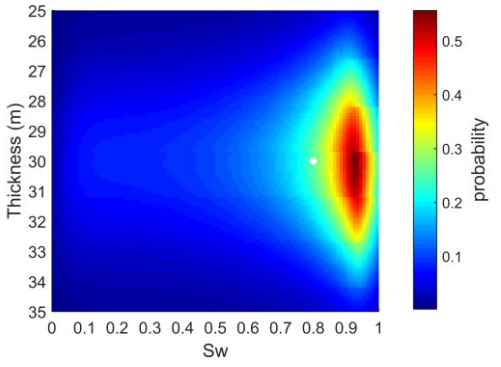

(d) Sw=80% Vp=3.04 km/s

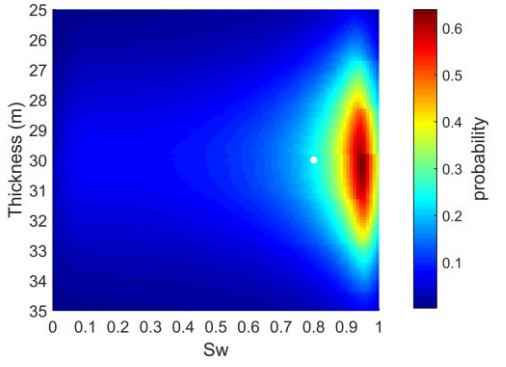

(e) Sw=80% Vp=3.05km/s

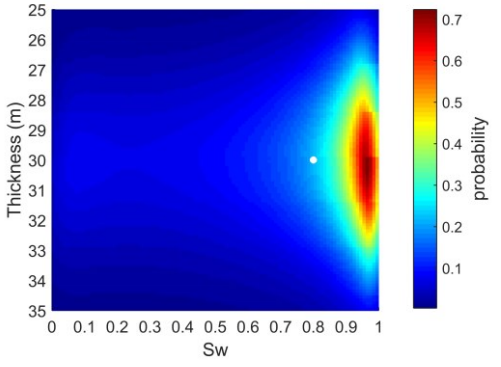

(f) Sw=80% Vp=3.06 km/s

Figure 13. Posterior probability of h and S_w at varying well-log P-wave velocities for the reservoir saturated by 80% water. The true value of h (30m) and S_w (80%) is marked with white circle.

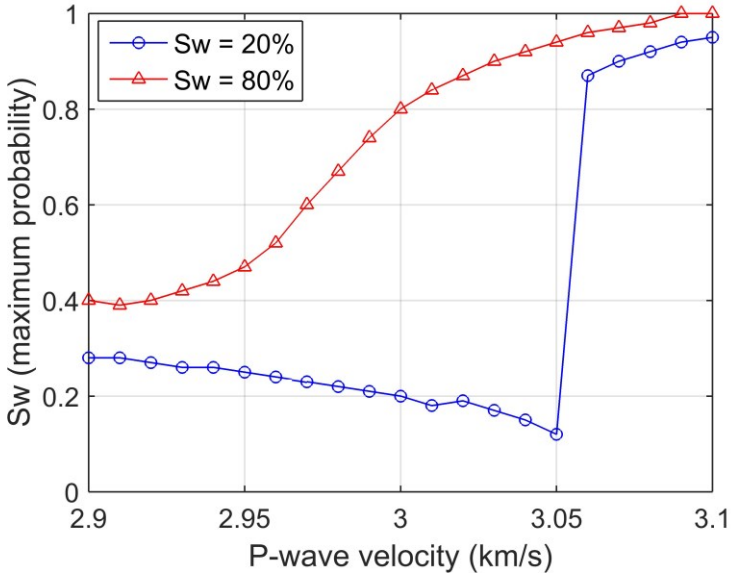

Figure 14. S_w with maximum posterior probability versus varying well-log P-wave velocities. The 20% water saturation case is indicated by blue circle, and the 80% water saturation case is labelled with red triangle. The true P-wave velocity is 3 km/s.

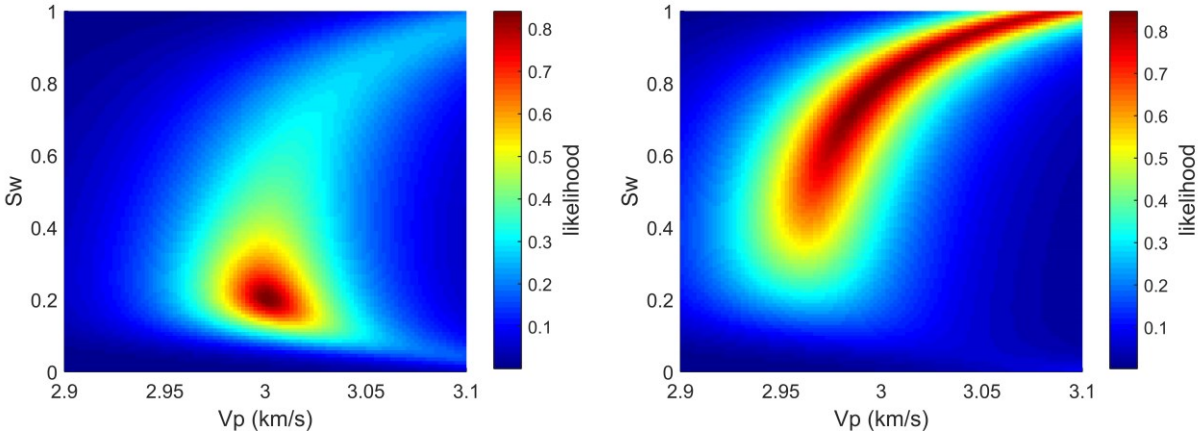

(a) Sw=20%

(b) Sw=80%

Figure 15. The likelihood function of water saturation S_w and P-wave velocity at fixed reservoir thickness of 30 meters. (a) 20% water case. (b) 80% water case.

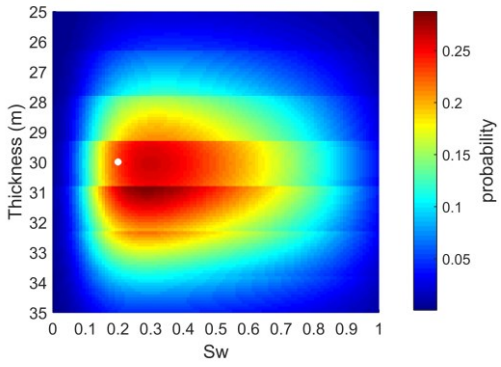

(a) Sw=20% ε=0.07

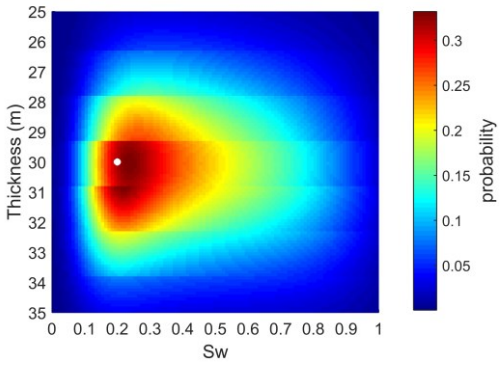

(b) Sw=20% ε=0.09

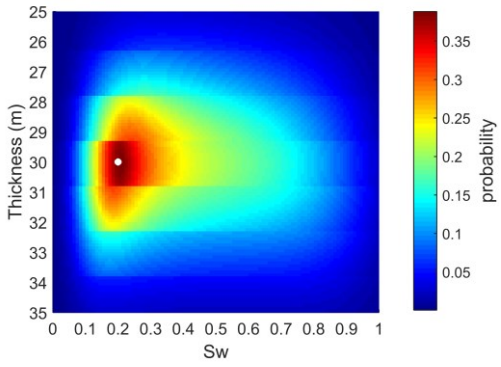

(c) Sw=20% ε=0.10

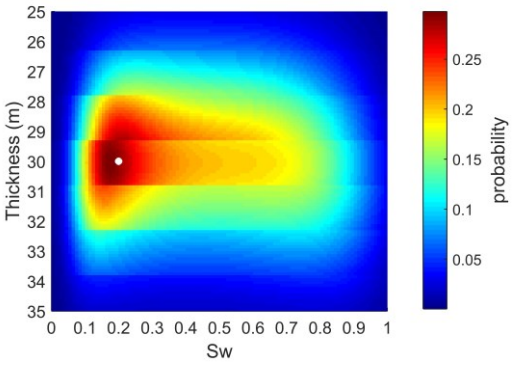

(d) Sw=20% ε=0.11

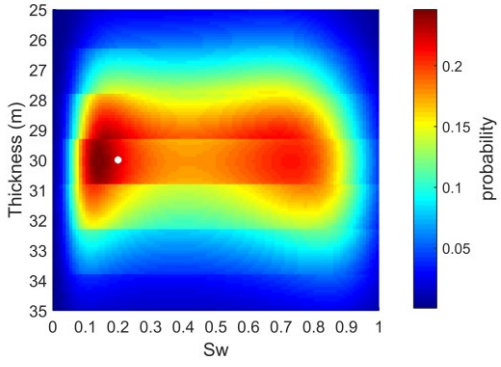

(e) Sw=20% ε=0.12

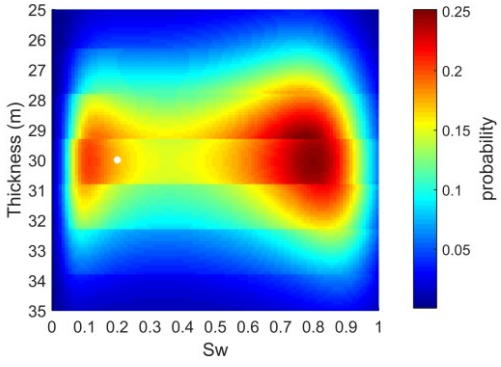

(f) Sw=20% ε=0.13

Figure 16. Posterior probability of h and S_w at varying rock physics parameter crack densities ε for the reservoir saturated by 20% water. The true value of h (30m) and S_w (20%) is marked with white circle.

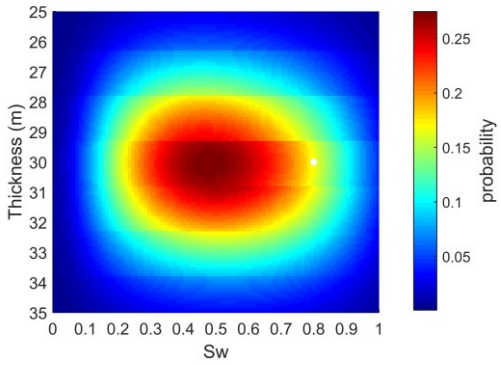

(a) Sw=80% ε=0.07

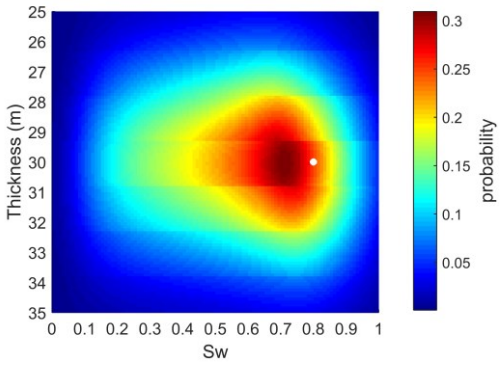

(b) Sw=80% ε=0.09

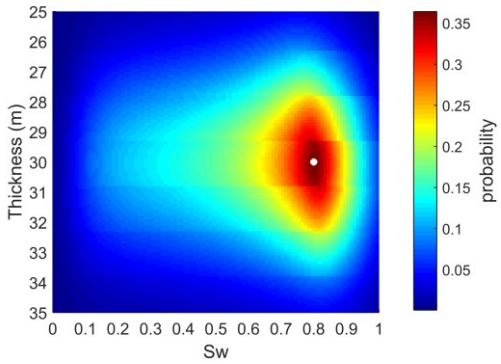

(c) Sw=80% ε=0.10

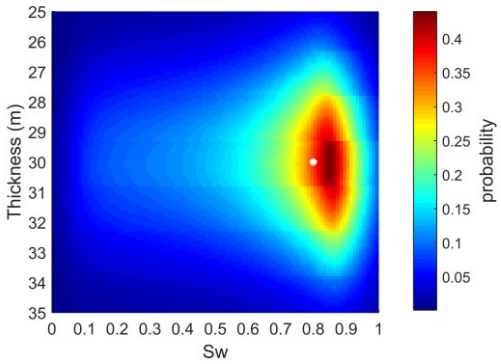

(d) Sw=80% ε=0.11

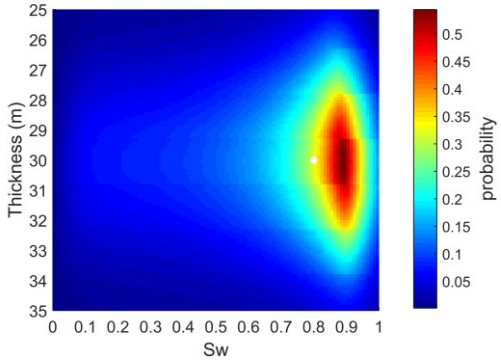

(e) Sw=80% ε=0.12

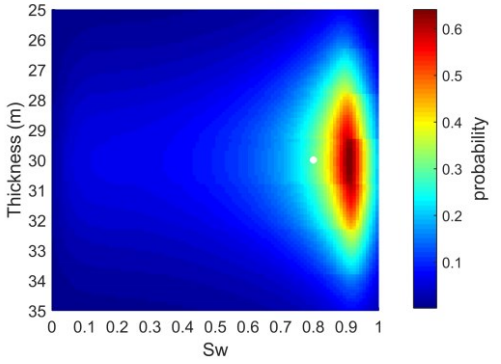

(f) Sw=80% ε=0.13

Figure 17. Posterior probability of h and S_w at varying rock physics parameter crack densities ε for the reservoir saturated by 80% water. The true value of h (30m) and S_w (80%) is marked with white circle.

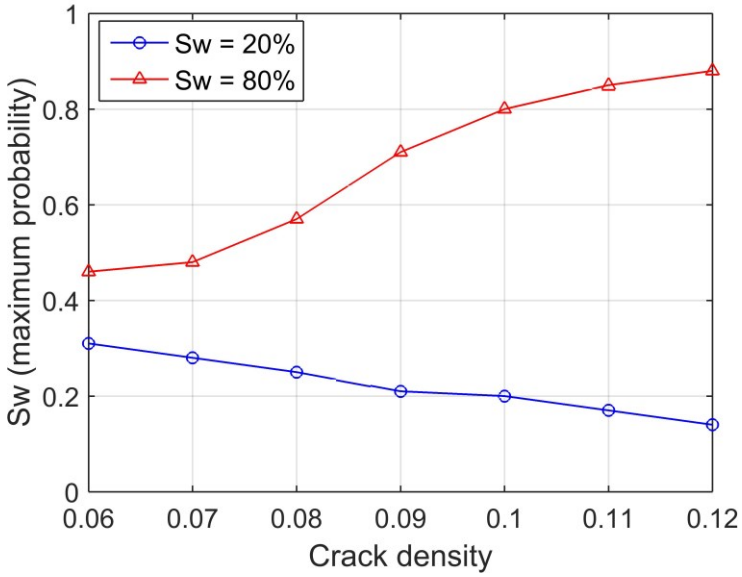

Figure 18. S_w with maximum posterior probability versus varying crack densities. The 20% water saturation case is indicated by blue circle, and the 80% water saturation case is labelled with red triangle. The true crack density is 0.1.